convective center to also move to the southeast. Another possibility is that the warming of Eurasia and the consequent strengthening of the monsoon has effectively pushed the Walker cell further away, to the southeast. Again, this is hard to test with data but could be checked with sufficiently realistic models.

We suggest that both the shift in Walker circulation anomalies and the enhanced land-sea gradient are countering the historical monsoon-ENSO inverse relationship, keeping the monsoon at a normal level despite increased ENSO activity in the recent decades. This recent breakdown in the ENSO-monsoon connection is without precedent in the historical record. It is noteworthy that all the links we present are consistent with the idea that the root cause is the recent warming trend. This may all be because of natural variability, but there is the intriguing possibility that global warming has broken the link between ENSO and the monsoon by preventing monsoon failure.

References and Notes

1. H. F. Blanford, *Proc. R. Soc. London* **37**, 3 (1884).
2. G. T. Walker, *Q. J. R. Meteorol. Soc.* **22**, 223 (1918).
3. P. J. Webster *et al.*, *J. Geophys. Res.* **103**, 14451 (1998).
4. P. J. Webster, in *Monsoons*, J. S. Fein and P. L. Stephens, Eds. (Wiley, New York, 1987), pp. 275–332.
5. J. Shukla, in (*4*), pp. 399–464.
6. G. B. Pant and B. Parthasarathy, *Arch. Meteorol. Geophys. Bioklimatol. Ser. B* **29**, 245 (1981); E. M. Rasmusson and T. H. Carpenter, *Mon. Weather Rev.* **111**, 517 (1983); C. F. Ropelewski and M. S. Halpert, *ibid.* **115**, 1606 (1987).
7. B. Parthasarathy, K. Rupa Kumar, A. A. Munot, *J. Clim.* **4**, 927 (1991); K. Krishna Kumar, M. K. Soman, K. Rupa Kumar, *Weather* **50**, 449 (1995); V. Krishnamurthy and B. N. Goswami, *COLA Report No. 62* (Center for Ocean-Land-Atmosphere, Calverton, MD, 1998).
8. K. Krishna Kumar, R. Kleeman, M. A. Cane, B. Rajagopalan, *Geophys. Res. Lett.* **26**, 75 (1999).
9. J. Shukla and D. A. Paolino, *Mon. Weather Rev.* **111**, 1830 (1983); S. Hastenrath, *Climate Dynamics of the Tropics* (Kluwer Academic, Dordrecht, Netherlands, 1991).
10. K. R. Sperber and T. N. Palmer, *J. Clim.* **9**, 2727 (1996).
11. The following data sets were used in this study: (i) All-India summer (June to September) monsoon rainfall during 1856–1997 [B. Parthasarathy, K. Rupa Kumar, A. A. Munot, *Theor. Appl. Climatol.* **49**, 217 (1994); N. A. Sontakke, G. B. Pant, N. Singh, *J. Clim.* **6**, 1807 (1993)]. (ii) The equatorial Pacific (NINO3) SST anomalies during 1856–1997. NINO3 area (5°S-5°N and 150°W-90°W) SST anomalies were obtained from the grid-point data of A. Kaplan *et al.* [*J. Geophys. Res.* **103**, 18567 (1998)] for the era 1856–1949, and those during 1950–1997 are taken from the Climate Prediction Center, Washington, DC (http://nic.fb4.noaa.gov/data/cddb/). The correlation between the two NINO3 series during the common period of 1951–90 is 0.97. (iii) Monthly velocity potential at 200 hPa during 1958–97 were obtained from the NCEP/NCAR reanalysis [E. Kalnay *et al.*, *Bull. Am. Meteorol. Soc.* **77**, 437 (1996)]. (iv) The 5° by 5° surface temperature anomalies on land as well as oceans during 1871–1997 [P. D. Jones, *J. Clim.* **7**, 1794 (1994); D. E. Parker, C. K. Folland, M. Jackson, *Clim. Change* **31**, 559 (1995)]. The anomalies are with respect to the 1961–90 climatology.
12. The rainfall and the NINO3 series are resampled [B. Efron, *Ann. Stat.* **7**, 1 (1979)] 1000 times in random 21-year chunks. For each resample, the correlation between the rainfall and NINO3 series is computed. The 5th and 95th percentile of these 1000 correlation coefficients provide 95% confidence limits of −0.45 and −0.70, respectively. The correlations in the recent decades fall outside this range, indicating that the relationship in this period is significantly different from the rest of the record.
13. J. Ju and J. Slingo, *Q. J. R. Meteorol. Soc.* **121**, 1133 (1995); G. A. Meehl and J. M. Arblaster, *J. Clim.* **11**, 1356 (1998).
14. D. J. Hahn and J. Shukla, *J. Atmos. Sci.* **33**, 2461 (1976); S. Yang, *Int. J. Climatol.* **16**, 125 (1996); M. Shankar Rao, K. M. Lau, S. Yang, *ibid.*, p. 605.
15. T. P. Barnett, L. Dümenil, U. Schlese, E. Roeckner, M. Latif, *J. Atmos. Sci.* **46**, 661 (1989).
16. T. Yasunari, A. Kitoh, T. Tokioka, *J. Meteorol. Soc. Jpn.* **69**, 473 (1991); G. A. Meehl, *Science* **266**, 263 (1994); A. D. Vernekar, J. Zhou, J. Shukla, *J. Clim.* **8**, 248 (1995); X. Shen, M. Kimoto, A. Sumi, *J. Meteorol. Soc. Jpn.* **76**, 217 (1998).
17. N. Nicholls *et al.*, in *Climate Change 1995: IPCC Second Assessment*, J. T. Houghton *et al.*, Eds. (Cambridge Univ. Press, Cambridge, 1996), pp. 133–192.
18. A. Bamzai and J. Shukla, *COLA Report No. 53* (Center for Ocean-Land-Atmosphere, Calverton, MD, 1998).
19. R. K. Verma, K. Subramaniam, S. S. Dugam, *Proc. Indian Acad. Sci. (Earth Planet. Sci.)* **94**, 187 (1985).
20. Model simulations [A. Kumar, A. Leetmaa, M. Ji, *Science* **266**, 632 (1994)] reproduce the observed Eurasian warming in the recent decades when forced by global SSTs associated with strong and weak ENSO situations. However, the mechanisms for this link are not clear. A causal link in the opposite sense may also exist (*15*), where Eurasian snow cover anomalies may influence ENSO.
21. G. A. Meehl and W. M. Washington, *Science* **260**, 1101 (1993); B. Bhaskaran, J. F. B. Mitchell, J. R. Lavery, M. Lal, *Int. J. Climatol.* **15**, 873 (1995).
22. We thank C. Ropelewski, R. Kleeman, S. Zebiak, and Y. Kushnir for useful discussions and comments. Supported by National Oceanic and Atmospheric Administration (NOAA) grant NA67GP0299. B.R. and M.A.C. were partially supported by NOAA grant NA56GP0221. This is Lamont-Doherty Earth Observatory contribution 5937.

5 March 1999; accepted 11 May 1999

Gold Solubility in Supercritical Hydrothermal Brines Measured in Synthetic Fluid Inclusions

Robert R. Loucks[1]* and John A. Mavrogenes[1,2]

Dissolved gold contents in chloride brines that were experimentally saturated with gold, magnetite, iron sulfides, orthoclase, and muscovite at 550° to 725°C and 100 to 400 megapascals are reported here. Microsamples of the fluid were isolated at the experimental temperature and pressure as fluid inclusions in quartz. Individual fluid inclusions were opened by laser ablation and analyzed by inductively coupled plasma mass spectrometry. The results show that gold solubility as sulfide species in supercritical brines is far higher than previously supposed. Dissolved gases such as molecular hydrogen sulfide that are ineffective metal-complexing agents at low pressures evidently become highly effective at high pressures.

More than four-fifths of the world's historic gold production has come from mesothermal- and porphyry-type ore deposits (*1, 2*) in which aqueous fluids at temperatures (*T*) and pressures (*P*) well above the critical point of water are implicated in metal transport (*3*). Gold transport and deposition mechanisms in these deposits have been conjectural, largely because the fluid's gold-carrying capacity and identity of the dissolved gold species were undetermined at magmatic temperatures and contentious at 250° to 400°C. Here we report experimental identification of the gold solute species and solubility in supercritical fluids in the range of *T* and *P* in which hydrothermal fluids extract ore-forming solutes from granitoid magmas or rocks undergoing amphibolite- to granulite-facies metamorphism.

We isolated fluid samples from mineral reactants at the experimental *T* and *P* as large fluid inclusions ($\geq 75 \times 500$ μm) trapped in quartz in pits predrilled by laser ablation and sealed by quartz overgrowth during the experiment (*4*). The analysis used laser-ablation extraction of an individual fluid inclusion. The laser beam diameter was adjusted to include the immediately adjacent host quartz and so extract all quench precipitates in the inclusion. The ablation product was analyzed by inductively coupled plasma mass spectrometry (ICPMS) (*5*). Previous solubility studies with synthetic fluid inclusions used the precracked-quartz synthesis technique developed by Shelton and Orville (*6*) and were limited to ordinary microscope observation of thermally induced phase changes in solutions of extremely soluble salts (*7*). Quantitative measurement (to better than ±15%) of the solubilities of sparingly soluble solids in the tiny inclusions (typically <40 μm) produced by the cracked-quartz synthesis technique had to await development of sensitive ICPMS laser-ablation techniques (*8*).

In experiments assessing the role of Au-Cl species in sulfidic brine, we varied the chloride content in starting solutions at buffered activities of H^+, H_2, and H_2S, at constant

---

[1]Research School of Earth Sciences, [2]Department of Geology, Australian National University, Canberra, A.C.T. 0200, Australia.

*To whom correspondence should be addressed. E-mail: Robert.Loucks@anu.edu.au

$T = 625$°C and $P = 370$ MPa (Table 1, runs 5 and 6) (*9*). As Cl varied from 0 to 1 *m* HCl + KCl, gold solubility varied insignificantly—from 761 ± 107 to 728 ± 103 ppm—consistent with earlier gold solubility measurements in sulfidic chloride brines at 250° to 500°C (*10–13*). Au-Cl complexes are not important in pyrite-saturated brines at any geologically relevant pH or redox state.

To assess the dependence of gold solubility on the H_2S content of the fluid, we varied the FeS and FeS_2 concentrations in the buffer assemblage pyrrhotite + magnetite ± pyrite (*14, 15*). These solids also buffer the H_2/H_2O ratio in the fluid. The activities of these components and the measured Au molality [$m_{Au(aq)}$] in fluid inclusions constrain the ratio of elements in the aqueous Au sulfide species by determining the coefficient "*n*" in the equilibrium:

$$Au(c) + nH_2S(g) = AuHS(H_2S)_{n-1}{}^0(aq) + 0.5H_2(g) \qquad (1)$$

This gives $AuHS^0(aq)$ if $n = 1$ or $AuHS(H_2S)^0(aq)$ if $n = 2$, for example. The $m_{Au(aq)}$ and relative fugacities or activities (a_i) of gases in Eq. 1 are related to its equilibrium constant K_1 by $\log m_{Au(aq)} + 0.5 \log a_{H_2(g)} = n \log a_{H_2S(g)} + [\log K_1 - \log \gamma_{Au(aq)} + \log a_{Au(c)}]$. γ_{Au} is the activity coefficient of dissolved gold; a_{H_2} and a_{H_2S} have gaseous reference states for thermodynamic accuracy (*16*). At saturation with crystalline gold, Au(c), at fixed *P*, *T*, and chlorinity, the terms in square brackets are constant. In Fig. 1A, the slope is found by linear regression to be $n = 4$ (*17*).

Experiments in the system S–H_2O imply that thiosulfate may be abundant at $T >$ 300°C (*18*). Another reaction that can produce an aqueous gold complex with four S atoms per Au atom is

$$Au(c) + 4H_2S(g) + 6H_2O = Au(HS_2O_3)(H_2S_2O_3)^0(aq) + 8.5H_2(g) \qquad (2)$$

Gold solubility by Eqs. 1 and 2 differs greatly in sensitivity to varied $a_{H_2(g)}$, so experiments can assess the relative importance of the two alternatives. Activities of species in Eq. 2 are related to its equilibrium constant K_2 by $4 \log a_{H_2S(g)} - \log m_{Au(aq)} = 8.5 \log a_{H_2(g)} - [\log K_2 + 6 \log a_{H_2O}]$ (the bracketed term is about constant at any *T* and *P*). In contrast, Eq. 1 corresponds to $4 \log a_{H_2S(g)} - \log m_{Au(aq)} = 0.5 \log a_{H_2(g)} - \log K_1$. A plot of terms on the left side of the equality against $\log a_{H_2(g)}$ must show a much steeper slope (to 8.5) in intervals in which a thiosulfate complex is substantial. Our data (Fig. 1B) show that over a redox range extending nearly to hematite saturation at $\log a_{H_2(g)} = -0.99$, the slope does not deviate perceptibly from 0.5. The experiments are consistent with gold dissolution according to Eq. 1 over the entire range of $a_{H_2(g)}$. Gold-thiosulfate complexes can mobilize gold in surficial weathering regimes (*19*), but we see no effect of thiosulfate in supercritical fluids over a wide range of redox conditions.

The remaining uncertainty in the identity of the aqueous Au complex is its electric charge. In fluids of variable acidity, the neutral and charged candidates are related by ionization reactions of the type $AuHS(H_2S)_{n-1}{}^0(aq) = H^+ + Au(HS)_2(H_2S)_{n-2}{}^-(aq)$, giving $Au(HS)_2{}^-(aq)$ if $n = 2$, for example. By this, gold solubility must increase tenfold as pH increases by 1 unit at constant *T*, *P*, $a_{H_2S(g)}$, and $a_{H_2(g)}$. But gold solubility by Eq. 1 is independent of pH. The test to determine if charged ions and pH are important was done by paired experiments at constant *T*, *P*, $a_{H_2(g)}$, and $a_{H_2S(g)}$, as pH was varied from acidic to alkaline by varying the chloride content from 0 to 1 molal. Runs 5 and 6 in Table 1 show that a variation of 2.4 pH units in this pair of runs was accompanied by no substantial change in dissolved Au (728 ± 103 ppm Au at pH = 4.3; 761 ± 107 ppm Au at pH = 6.7). So the dissolved Au was uncharged (*20*). Gold solubility is insensitive to pH variations within the geologically relevant range at

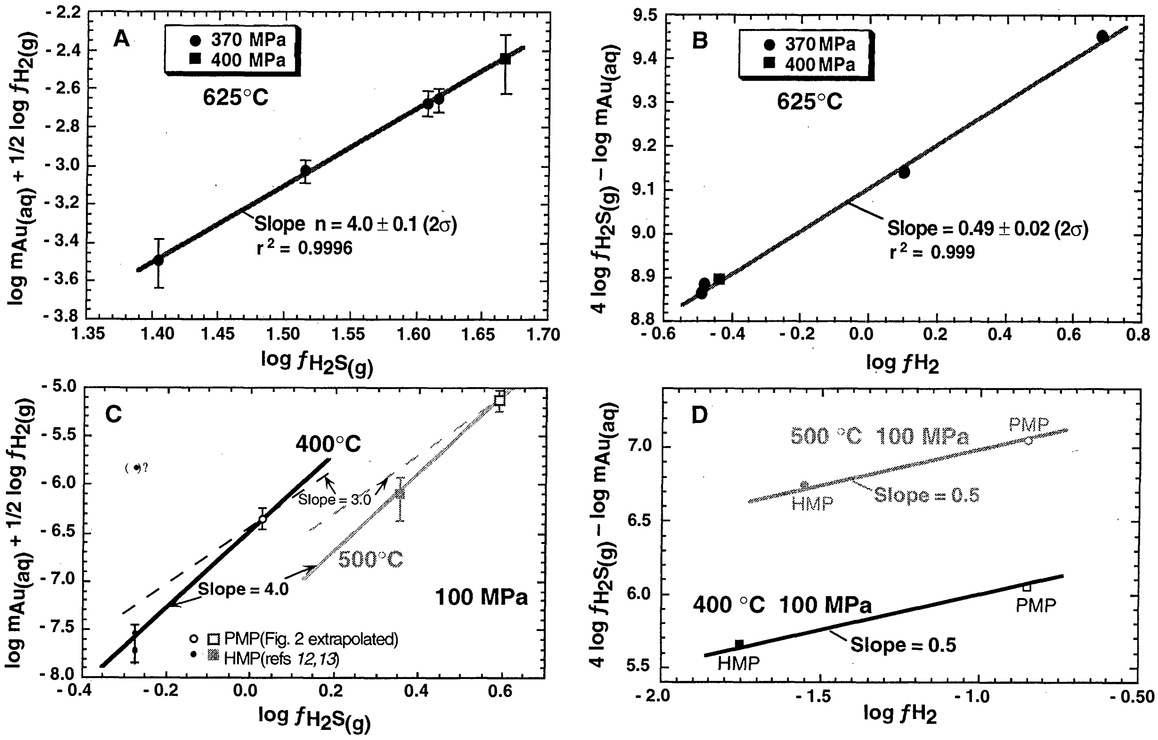

Fig. 1. Graphical evaluation of the proportions of participating species in the gold dissolution reaction, Eq. 1. (**A**) Terms on the left side of Eq. 1 are plotted against $\log a_{H_2S(g)}$ for each of the five experiments at 625°C and 370 to 400 MPa (Table 1). The slope is $n = 4$, which is the number of H_2S molecules required to supply the S bonded to one atom of Au in solution. Error bars represent the uncertainty in *T*, *P*, m_{Au}, and a_{FeS}; uncertainties in thermodynamic data for the buffer equilibria do not affect evaluation of the slope (*36*). (**B**) Data from Table 1 for five runs at 625°C and 370 to 400 MPa yield a slope of 0.5, so 0.5 is the number of H_2 molecules released from 4 H_2S as a by-product of dissolving one atom of Au; the other seven H atoms are evidently bonded in the Au complex. (**C**) Open symbols are values obtained by extrapolation of a least squares fit of experimental results at nine *P-T* coordinates [Table 1 and (*12*)] for Au solubility in the presence of pyrrhotite + magnetite + pyrite (PMP). Filled symbols are experimentally determined values (*12, 13*) in the presence of the hematite + magnetite + pyrite (HMP) buffer, for which there are 15 experiments at 500°C and three in the bracketed interval at 400°C, plus an outlier that was not considered. Again, the slope indicates an atomic ratio S:Au = 4 in the aqueous gold complex. (**D**) Open and filled symbols have the same meaning as in (C). Results in (A) to (D) robustly constrain the stoichiometry of Eq. 1 and thereby constrain the stoichiometry of the aqueous gold complex to contain four S atoms and seven H atoms per Au atom over the interval 100 to 400 MPa and 400° to 625°C and a large range of the redox ratio a_{H_2}/a_{H_2O}.

625°C and 370 to 400 MPa.

Incorporating published data (*12, 13*) at 400° to 500°C, 100 MPa, we obtained slopes constraining the reaction coefficient of H_2S as 4 (Fig. 1C) and of H_2 as 0.5 (Fig. 1D). Those coefficients identify the atomic proportions in the dominant gold species as S:Au = 4 and H:Au = 7. From at least 625° to 400°C, 400 to 100 MPa, a broad range of m_{H_2S}, redox conditions spanning reduced (pyrrhotite stable without pyrite) to oxidized (hematite stable), and <30 to >1180 ppm Au, gold solubility in iron sulfide–saturated brines is controlled by a single equilibrium:

$$\mathrm{Au(c)} + 4\mathrm{H_2S(g)} = \mathrm{AuHS(H_2S)_3{}^0(aq)} + \tfrac{1}{2}\mathrm{H_2(g)} \qquad (3)$$

Experimentally determined activities of chemical components [Table 1 and (*12, 13*)] yield thermodynamic parameters of Eq. 3 by fitting the tabulated activities to an equation of the form

$$\ln m_{\mathrm{Au(aq)}} + \ln \gamma_{\mathrm{Au(aq)}} + \tfrac{1}{2} \ln a_{\mathrm{H_2(g)}} - 4 \ln a_{\mathrm{H_2S(g)}} = \ln K_3 = \mathrm{A} + \frac{B}{T} + C \ln T + D\frac{P}{T} \qquad (4)$$

The least squares fit yields values for the coefficients A, B, C, and D (*21*) that correspond to the changes in entropy ($\Delta_r S^\circ_{T_0} = -273 \pm 3$ J/K), enthalpy ($\Delta_r H^\circ_{T_0} = -105{,}353 \pm 2361$ J), heat capacity ($\Delta_r C^\circ_p = 0 \pm 1$ J/K), and volume of reaction ($\Delta_r V^\circ = 4.4 \pm 0.2$ J/bar) in Eq. 3. Because $\Delta_r C^\circ_p \simeq 0$, $\Delta_r S^\circ$ and $\Delta_r H^\circ$ do not vary with choice of T_0. From these reaction parameters, the partial molal properties of the $\mathrm{AuHS(H_2S)_3{}^0(aq)}$ molecule were obtained from difference relations such as $\bar{S}^\circ_{\mathrm{AuHS(H_2S)_3{}^0(aq)}} = \Delta_r S^\circ_T - 0.5\, S^\circ_{\mathrm{H_2(g)}} + S^\circ_{\mathrm{Au(c)}} + 4S^\circ_{\mathrm{H_2S(g)}}$ for entropy and of the same form for enthalpy and heat capacity. Gases do not participate in the volume analog $\bar{V}^\circ_{\mathrm{AuHS(H_2S)_3{}^0(aq)}} = \Delta_r V^\circ_T + V^\circ_{\mathrm{Au(c)}}$ (*22*). Such difference relations work well here because these properties of Au(c), H_2S(g), and H_2(g) are accurately known (*15*). The variation of the partial molal enthalpy, entropy, heat capacity, and volume of $\mathrm{AuHS(H_2S)_3{}^0(aq)}$ with T and P were fitted by Helgeson-Kirkham-Flowers equation-of-state parameters (*23*) to permit accurate extrapolation for geochemical modeling and to generate the $\mathrm{AuHS(H_2S)_3{}^0(aq)}$ solubility contours in Fig. 2. Parameters that yield the curves for $\mathrm{AuHS^\circ(aq)}$ in Fig. 2 were also derived (*24*).

In Archean greenstones and modern oceanic basalts, typical background Au contents are 0.7 to 2 ppb (*25*). Even with 100% extraction efficiency, fluids emitted from such rocks by amphibolite-facies devolatilization reactions would contain ≲0.2 ppm Au. The much higher content of dissolved gold needed to initiate precipitation at $T \geq 550$°C and $P \geq 200$ MPa (Fig. 2) is unlikely to be available unless the fluid is remobilizing gold ore formed earlier at lower T, even if the fluid's a_{H_2}/a_{H_2S} ratio is extremely high (Eq. 3). A rough upper limit on a_{H_2}/a_{H_2S} is represented by the iron-arsenide-sulfide-oxide assemblage loellingite + arsenopyrite + pyrrhotite + magnetite (LAPM), which occurs in some upper-amphibolite- to granulite-facies gold ores (600° to 700°C) (*26*). Desulfidation of the fluid from pyrite to loellingite stability at constant 370-MPa P_{H_2O} and 625°C, for example, spans most of the geologically accessible range but causes a reduction of gold solubility from ~761 ± 107 ppm Au on the PMP buffer (Table 1, run 6) to ~14 ± 7 ppm Au on the LAPM buffer (*27*). The latter saturation requirement is orders of magnitude beyond the range available to fluids by leaching common rocks or by exsolution from granitoid magmas. Probably all gold lodes having upper-amphibolite- to granulite-facies mineral assemblages are metamorphosed ores, incidentally recrystallized and locally remobilized at conditions that do not represent processes responsible for primary gold enrichment. Another implication of the PMP-LAPM comparison is that desulfidation of the fluid (by pyritization of ferruginous rocks, for example) may help focus gold ore precipitation, but it is of second-order importance compared with the drastic decrease in gold solubility as fluid migrates from mid-amphibolite- to mid-greenschist-facies T and P (or thermal equivalents around epizonal plutons). Imagine a cooling fluid-flow path corresponding to a horizontal line at ~0.2 ppm Au on Fig. 2, which extends leftward to meet a saturation contour at ~400°C. In just the next 60°C or so, >90% of the dissolved gold precipitates in response to cooling alone.

Metamorphic waters ascending through the ductile-to-brittle transition, usually at ~425° to 375°C, can experience steep decompression gradients (*28*). A transition from lithostatic to hydrostatic load at 400°C and 10-km depth, for example, would decompress the fluid by ~200 MPa, causing gold solu-

Table 1. Run conditions and durations and measured and calculated compositions of 89 samples of supercritical fluids trapped as gold-saturated fluid inclusions.

Run conditions*					Measured concentrations†				Calculated concentrations‡				Thermodynamic activities§						
Exp	T (°C)	P (MPa)	Time (days)	Buffer Fe-S-O	ΣCl(aq) (m)	n fi's	U/Th	Au ± 95% C.L. (ppm)	$FeCl_2^\circ$ (m)	KCl° (m)	HCl° (m)	K^+(aq) (m)	pH fluid	H_2O gas	H_2S gas	H_2 gas	SO_2 gas	FeS cryst	FeS_2 cryst
1	725	110	24	PoMtPy	1	12	7.34	135 ± 13	–	–	–	–	–	~848	~21.9	~0.092	–	0.384	1.000
2	625	110	28	PoMtPy	1	12	5.87	61 ± 15	0.36	0.13	0.1320	0.014	5.35	716	12.1	0.118	11.2	0.441	1.000
3	550	310	35	PoMtPy	1	1	(1.2)	84 ± –	0.14	0.18	0.0013	0.55	4.20	1353	17.6	0.309	0.22	0.492	1.000
4	625	400	35	PoMtPy	1	2	6.32	1180 ± 390	0.22	0.17	0.0020	0.39	4.26	2350	46.4	0.363	16.0	0.441	1.000
5	625	370	23	PoMtPy	1	8	5.43	728 ± 103	0.24	0.16	0.0021	0.36	4.27	2088	40.5	0.325	15.5	0.441	1.000
6	625	370	28	PoMtPy	0	18	1.99	761 ± 107	0	0	0	0.0006	6.71	2105	41.3	0.331	15.5	0.441	1.000
7	625	370	35	PoMt	1	26	6.02	29 ± 8	0.30	0.12	0.0016	0.28	4.36	2088	25.4	4.83	0.003	0.680	0.065
8	625	370	28	PoMt	1	10	5.99	167 ± 23	0.27	0.14	0.0018	0.31	4.32	2088	32.9	1.25	0.22	0.560	0.268

*See (*4*) for procedural details. "Exp" gives the experiment number. "Time" column represents run duration, not equilibration time between reactants and the fluid sample. Our rate studies at 625°C and 370 MPa show that predrilled, large laser pits seal over (isolating a fluid sample from reactants) 10 to 30 days into the run, whereas microcracks heal and isolate fluid samples a few hours to a few days after the run begins. Both inclusion types were obtained and analyzed in most runs. The two types of inclusions represent widely varying fluid-mineral reaction times (that is, the 89 inclusions are 89 quasi-independent experiments with different reaction durations), but there is no systematic compositional difference between the two types within individual runs. Buffer minerals: Po, pyrrhotite; Mt, magnetite; Py, pyrite. †The number "n" of fluid inclusions (fi's) analyzed in each run is shown. Quantification of Au is relative to the known U and Th concentrations in fluid inclusions (*5*). Confidence limits (C.L.) about the mean are calculated from the t statistic as $t \times SD/\sqrt{n}$. A criterion for a satisfactory fluid-inclusion analysis is recovery of the appropriate U/Th ratio, to within the usual analytical error. In the 1 m Cl starting solution, the initial U/Th = 5.86; in the Cl-free starting solution, the initial U/Th = 1.90. Run 3 produced only one small inclusion, and its Th counts were near the detection limit; the 84 ppm Au value is from the U/Au count ratio. ‡Fe-K-H-Cl speciation is from simultaneously solving equations for charge balance, chloride mass balance, and mass action for homogeneous and heterogeneous equilibria, with equilibrium constants from published sources (*15, 33, 34*); $m_{\mathrm{FeCl}^+} <$ 0.0001 in all experiments. Activity coefficients in KCl solutions are calculated from an extended Debye-Hückel formulation (*35*). In Cl-bearing runs, $m_{\mathrm{Cl}^-} = m^+_{\mathrm{K}}$ to the third decimal place. In Cl-free run 6, $m^\circ_{\mathrm{KOH}} = 0.00001$; $m_{\mathrm{OH}^-} = 0.00060$ (*20*). Run 1 at 725°C and 110 MPa is beyond the reliable calculation range of electrostatic and solvation properties of H_2O; ionization of KCl and HCl must be trivial in the 725°C experiment and its pH near neutral. §Unit-activity standard states are as follows: gases, the ideal gas at 1 bar and the temperature of interest; solids, the pure substance at the T and P of interest; and aqueous solutes, the hypothetical ideal 1 m solution at T and P of interest. Fugacities (gas activities) were calculated with thermodynamic data for Fe-S-O-H buffer equilibria from the SUPCRT92 database (*15*). FeS activity in pyrrhotite is according to Toulmin and Barton's calibration (*14*); pyrrhotite is $Fe_{0.9484}S$ in run 7 and $Fe_{0.9337}S$ in run 8. cryst, crystalline.

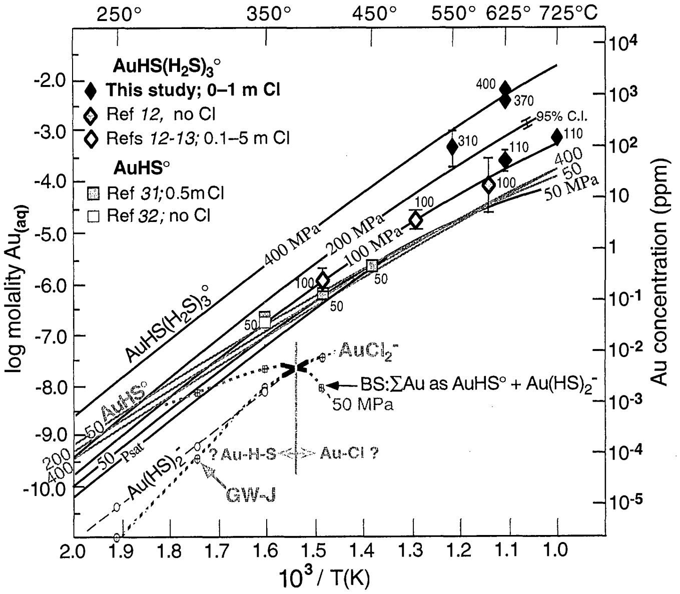

Fig. 2. Contributions by various complexes to the overall solubility of gold vary with *T* and *P* in chloride brine buffered by orthoclase + muscovite + quartz (OMQ) and PMP. The *P* of each experiment is labeled beside symbols having SE brackets shown if they are longer than the symbol. Shaded symbols represent measured Au contents in experiments with the PMP buffer [Table 1 and (*12, 13, 31*)]; open symbols represent gold-solubility values calculated for the PMP and OMQ buffers with equilibrium constants (*K*'s) measured at the same *T* and *P*. White diamonds are values calculated for the PMP buffer with *K*'s calibrated by experiments (*12, 13*) on the HMP buffer at 100 MPa, 400° and 500°C, in which $AuHS(H_2S)_3^{\circ}(aq)$ was identified (Fig. 1) as the main complex. Its solubility contours (continuous black lines) from steam saturation (P_{sat}) to 400 MPa are generated from its equation-of-state parameters derived in this study (*23*). Squares represent experiments at 50 MPa and 350° to 450°C, in which the $AuHS^{\circ}(aq)$ complex was found to predominate (*31, 32*). Curve BS is the Au solubility, chiefly as $AuHS^{\circ}(aq)$ in 1 *m* KCl at 50 MPa according to *K*'s reported by Benning and Seward (*37*). They are incompatible with the other plotted data for Au-H-S species and have been criticized at length by Gibert *et al.* (*31*). They are excluded from the 25° to 450°C, 0.1 to 50 MPa data set thermodynamically analyzed (*24*) to generate the isobaric $AuHS^{\circ}(aq)$ solubility contours (solid gray lines). The $AuHS^{\circ}(aq)$ contour at P_{sat} (not plotted) is visually indistinguishable from its 50-MPa counterpart. The contours show that at 400 MPa, $AuHS(H_2S)_3^{\circ}(aq)$ predominates by ~1 to 3 log units over the whole *T* range; it predominates at 200 MPa down to ~250°C, where it intersects the 200-MPa contour of $AuHS^{\circ}(aq)$, which is higher at $T <$ 250°C. At 50 MPa, $AuHS^{\circ}(aq)$ predominates over most of the *T* range shown. The transition from $AuHS(H_2S)_3^{\circ}(aq)$ at high *T* and *P* to $AuHS^{\circ}(aq)$ at lower *T* and *P* is attributable to two factors: (i) H_2S availability as a complexing ligand increases with *T* by many log units, being controlled by iron sulfide solubility (*38*), and (ii) the $\Delta_r V^{\circ}$ of the reaction $AuHS^{\circ}(aq) + 3H_2S(aq) = AuHS(H_2S)_3^{\circ}(aq)$ is negative, and its magnitude becomes large at low pressures as solvated H_2S becomes more gaslike (*39*). Complexes of other metals with H_2S or HCl (or other solvated gases) probably have analogous pressure dependence, becoming unimportant at low *P* as the ligand's partial molal volume expands. $Au(HS)_2^-$ is a minor species under these buffer conditions, because of acidic pH in 1 *m* Cl solutions buffered by OMQ (*40*). The experimentally well constrained $AuCl_2^-$ trend labeled GW-J (*41*) (calculated for 1 *m* Cl brine, OMQ and PMP buffers) intersects the relatively flat to thermally retrograde BS trend. Presuming the BS trend to be valid for Au-H-S complexes, Gammons and Williams-Jones (*42*) concluded that Au-Cl complexes evidently account for Au transport and ore precipitation from iron sulfide–saturated chloride brines at *T* above the BS/GW-J intersection (heavy cross and queried labels beneath). But our new experiments and thermodynamic analysis of four other mutually consistent studies of gold solubility at 400° to 725°C and 50 to 400 MPa show that gold-hydrosulfide complexes remain predominant in iron sulfide–saturated chloride brines up to granite-solidus temperatures and high fluid chlorinity.

bility to decrease by ~90% because of *P* decrease alone (Fig. 2). Analogous effects must occur in hydrothermal fluids that exsolve at lithostatic *P* from crystallizing epizonal plutons and migrate into groundwater regimes at hydrostatic load, forming porphyry-type gold-copper ore shells in the *P* transition interval (*29*).

Of gold mined from metamorphic rock worldwide, >90% was precipitated between 250° and 450°C and 100 to 300 MPa (*2, 30*). By revealing the high gold-transport capacity (gold-saturation requirement) in supercritical aqueous fluids and by demonstrating strong *T* and *P* dependence of gold solubility, our experiments can account for the strong bias in historic gold production from subgreenschist- and greenschist-facies metamorphic rocks. The bias does not signify an overlooked potential for comparable production from high-temperature metamorphic rocks.

References and Notes

1. A. Sutton-Pratt, *Trans. Inst. Min. Metall. Sect. B* **105**, B3 (1996); R. H. Sillitoe, *Austr. J. Earth Sci.* **44**, 373 (1997).
2. C. J. Hodgson *et al.*, in *Giant Ore Deposits*, B. H. Whiting *et al.*, Eds. (Society of Economic Geologists, Lancaster, PA, 1993), pp. 157–211.
3. R. Powell, T. M. Will, G. N. Phillips, *J. Metamorph. Geol.* **9**, 141 (1991); G. Stevens, R. Boer, R. Gibson, *S. Afr. J. Geol.* **100**, 363 (1997); R. J. Goldfarb, L. W. Snee, W. J. Pickthorn, *Mineral. Mag.* **57**, 375 (1993).
4. Quartz crystals were prepared for fluid-inclusion entrapment by ablating pits 30 to 100 μm in diameter and ~500 to 1000 μm deep with a 193-nm excimer laser and by generating thermal-stress microcracks. The quartz crystal, silica powder, and ~50 mg of each buffer mineral were sealed in gold foil capsules with 200 μl of aqueous solution containing 0 or 1 *m* HCl and known Th and U contents. The 1 $m_{\Sigma Cl}$ starting solution had 44 ppm U, 7.5 ppm Th, and U/Th = 5.86; the 0 $m_{\Sigma Cl}$ solution had 65.5 ppm U, 34.5 ppm Th, and U/Th = 1.90. Capsules were run in cold-seal vessels at a selected *T* (±5°C) and *P* (±2 MPa). Optical and x-ray diffraction analysis confirmed survival of buffers. Quartz crystals were sectioned and polished to reveal fluid inclusions.
5. The quartz matrix is devoid of the solute elements of interest. During ICPMS analysis, instrument background counts were measured with the laser off for ~60 s, after which the laser ablated the capping quartz until the fluid-inclusion cavity was breached, releasing its contents into a stream of argon carrier gas. The signal is attenuated by capillary flow in the ICPMS inlet system to a duration of ~30 s, after which count rates return to background levels. The three-element mass spectrum was scanned in 0.4-s cycles. Ratios of background-corrected, time-integrated counts of Au, Th, and U (ratios of areas under peaks of count rate versus time) were recast as element-concentration ratios by reference to their relative ionization efficiencies measured in a certified standard silicate glass, NIST-610, containing 462 ppm U, 457 ppm Th, and 25 ppm Au [G. A. Uriano, *Certificate of Analysis for Standard Reference Materials 610, 611: Trace Elements in a Glass Matrix* (U.S. National Bureau of Standards, Gaithersburg, MD, 1982); N. J. G. Pearce *et al.*, *Geostan. Newslett.* **21**, 115 (1997)]. The Au/U and Au/Th part per million ratios in the fluid inclusion were multiplied by the U and Th contents of the starting solution to obtain apparent part per million Au values relative to U and Th. A criterion for a satisfactory analysis—and evidence that U and Th were completely retained in solution during an experiment and serve reliably as internal standards in the inclusions—is that the fluid inclusion's U/Th ratio, measured relative to NIST-610 glass, matches the U/Th ratio in the starting solution, to within the usual analytical precision for such tiny samples. The accuracy of this dual-internal-standard analysis protocol was assessed by analyzing quartz-hosted, unsealed fluid "pseudoinclusions" containing a standard solution. About 0.5 μg of solution prepared to contain 103 ppm Au, 43.4 ppm U, and 7.4 ppm Th (U/Th = 5.86) in 1 m_{HCl} was injected by nylon microsyringe into laser-ablated pits in quartz and then frozen in liquid N_2. The ice plus an annulus of quartz was laser-ablated and analyzed by ICPMS to simulate ablation and analysis of sealed fluid inclusions. Replicate analyses gave a mean (± 1 SD) U/Th = 5.8 (± 0.2), Au = 105 (± 11) ppm relative to Th, and Au = 107 (± 13) ppm relative to U as the internal standard. The 10 Au determinations gave a pooled mean of 106 ± 9 ppm Au at the 95% confidence limit. From the pseudoinclusion tests, we conclude that (i) the analytical result 106 ± 9 ppm agrees with the nominal 103 ppm Au weighed into the standard solution, so no matrix-related bias is evident between the ablated glass standard and the ablated quartz + standard fluid, and (ii) in submicrogram-size samples, our analytical precision for Au by this U-Th dual-internal-standard procedure is ±~8% of the actual value.
6. K. L. Shelton and P. M. Orville, *Am. Mineral.* **65**, 1233 (1980).
7. R. J. Bodnar and S. M. Sterner, in *Hydrothermal Experimental Techniques*, G. C. Ulmer and H. L. Barnes, Eds. (Wiley, New York, 1987), p. 423.
8. R. R. Loucks *et al.*, in *Research School of Earth Sciences Annual Report* (Australian National University, Canberra, 1995), pp. 138–140; A. Audétat *et al.*, *Science* **279**, 2091 (1998).
9. Gold dissolves in water by the reaction Au(c) + $H^+(aq) = Au^+(aq) + 0.5H_2(g)$. With a complexing ligand, L, it becomes $Au(c) + H^+(aq) + nL^{z-} = AuL_n^{1-nz}(aq) + 0.5H_2(g)$. We tested two ligands, H_2S and HCl. By Gibbs' phase rule, a system of two phases (fluid and crystalline gold) and five chemical components (Au, H^+, H_2, H_2S, and HCl) has 5 degrees of freedom, which are eliminated as follows. We fix *T* and *P* ($=P_{H_2O}$) in each experiment. HCl activity is fixed by the $m_{\Sigma Cl}$ of the starting solution, the ionization constant of HCl, and the buffer assemblage orthoclase + muscovite + quartz. The fluid's redox state (a_{H_2}/a_{H_2O})

is buffered by iron sulfides and magnetite. These also buffer the fluid's a_{H_2}/a_{H_2S} ratio, which is varied among experiments by varying the S/Fe ratio in pyrrhotite up to its pyrite-saturation limit.

10. J. J. Rytuba and F. W. Dickson, in *Problems of Ore Deposition, Fourth IAGOD Symposium* (Bulgarian Academy of Sciences, Varna, Bulgaria, 1977), pp. 320–326.
11. K.-I. Hayashi and H. Ohmoto, *Geochim. Cosmochim. Acta* **55**, 2111 (1991).
12. G. G. Likhoydov and I. Y. Nekrasov, *Dokl. Akad. Nauk SSSR* **323**, 294 (1992).
13. ———, *Dokl. Ross. Akad. Nauk* **336**, 380 (1994).
14. Pyrrhotite analyzed by electron microprobe. FeS activity is according to P. I. Toulmin and P. B. Barton Jr. [*Geochim. Cosmochim. Acta* **28**, 641 (1964)].
15. J. S. Johnson, E. H. Oelkers, H. C. Helgeson, *Comput. Geosci.* **18**, 899 (1992).
16. In the *P-T* range of our experiments, there is no experimental corroboration of calculated $a_{H_2(g)}$ and $a_{H_2S(g)}$ values in Table 1, but N. Kishima [*Geochim. Cosmochim. Acta* **53**, 2143 (1989)] measured $a_{H_2(g)}$ and $a_{H_2S(g)}$ in water saturated with pyrite + pyrrhotite + magnetite at 300° to 500°C and P_{sat} to 100 MPa. His results generally lie within 0.1 log unit of values calculated with the SUPCRT92 database (*15*), the basis of values in Table 1. For example, at 400°C and 100 MPa, Kishima measured fugacity $f_{H_2} = 0.013$ MPa and $f_{H_2S} = 0.091$ MPa, compared with 0.014 MPa f_{H_2} and 0.106 MPa f_{H_2S} from SUPCRT92.
17. It was not feasible to identify the stoichiometry of the gold complex spectroscopically, because the diamond-anvil hydrothermal cell—the only fluid receptacle presently available for optical-spectroscopic analysis in the *T* and *P* range of our experiments—is opaque to the ultraviolet wavelengths relevant to identification of gold-hydrosulfide complexes.
18. G. V. Bondarenko and Y. E. Gorbaty, *Geochim. Cosmochim. Acta* **61**, 1413 (1997); T. P. Dadze and V. I. Sorokin, *Geochem. Int.* **30**, 36 (1993).
19. J. G. Webster, *Geochim. Cosmochim. Acta* **50**, 1837 (1986).
20. In 1 $m_{\Sigma Cl}$, the pH buffer equilibrium is HCl(aq) + $1.5KAlSi_3O_8 = 0.5KAl_3Si_3O_{10}(OH)_2 + 3SiO_2$ + KCl(aq), which yields acidic pH because of HCl. Without Cl, the equilibrium is $H_2O + 1.5KAlSi_3O_8$ = KOH(aq) + $0.5KAl_3Si_3O_{10}(OH)_2 + 3SiO_2$, giving alkaline pH because of KOH(aq). The 2.4 units pH range (Table 1) is ≫tenfold larger than its uncertainty. We found gold solubility to be independent of pH, so the modest uncertainties in calculated pH [and in activities of $FeCl_2^\circ$(aq), KCl°(aq), HCl°(aq), and K^+ used only to calculate pH] are not propagated to identification of the stoichiometry of the gold complex nor to derivation of its thermodynamic properties.
21. In addition to Table 1, the regressed data set includes the following data derived from published experiments (*12, 13*): 400°C, 100 MPa, 0.034 ± 0.018 ppm Au (n = 3) on HMP buffer with $a_{H_2O(g)} = 262$, $a_{H_2S(g)} = 0.53$, and $a_{H_2(g)} = 0.018$; 500°C, 100 MPa, 0.91 ± 0.41 ppm Au (n = 15) on HMP buffer with $a_{H_2O(g)} = 459$, $a_{H_2S(g)} = 2.27$, and $a_{H_2(g)} = 0.028$; and 600°C, 100 MPa, 16 ± 10 ppm Au (n = 2) on PMP buffer at $a_{H_2O(g)} = 636$, $a_{H_2S(g)} = 9.43$, and $a_{H_2(g)} = 0.117$. Activities were calculated as in Table 1. Data were weighted according to estimated 1 SE confidence intervals as follows: $P \pm 2\%$; $T \pm 5°C$; uncertainties in $m_{\Sigma Au}$ as listed in Table 1 and given above for data of (*12, 13*); $a_{H_2(g)}$ and $a_{H_2S(g)}$ on PMP and HMP buffers are assumed to have no substantial uncertainty (*16*). We set $\gamma_{AuHS(H_2S)_3{}^0(aq)} = 1.0$. The fit of Eq. 4 to these experiments at 400° to 725°C and 100 to 400 MPa has $r^2 > 0.997$ and reduced $\chi^2 = 1.20$ for the parameters $A = \Delta_r S^\circ_{T_0}/R = -32.89 \pm 0.35$ (1σ), $B = -\Delta_r H^\circ_{T_0}/R = 12{,}671 \pm 284$ (1σ), $C = \Delta_r C^\circ_p/R = 0 \pm 1$ (1σ), and $D = -\Delta_r V^\circ/R = -0.532 \pm 0.025$ (1σ), wherein R is the gas constant. The fit retrieves the input log m_{Au} values with a SD = 0.052 log unit, which corresponds to the 95% confidence bracket of ±0.104 log unit shown in Fig. 2 for black solubility contours at ~200 to 400 MPa, 500° to 700°C.
22. Use of a gaseous, rather than solvated, reference state for H_2 and H_2S avoids propagating the relatively large uncertainties in volumes of the solvated molecules to derivation of the partial molal volume of the aqueous gold complex.
23. Thermodynamic equation-of-state parameters for $AuHS(H_2S)^\circ_3$(aq) are presented here in notation and units consistent with the SUPCRT92 computer program and thermodynamic database (*15*). As described by E. L. Shock, H. C. Helgeson, and D. A. Sverjensky [*Geochim. Cosmochim. Acta* **53**, 2157 (1989)], the partial molal Gibbs free energy of formation (ΔG) of an uncharged aqueous solute at any T and P differs from its value at reference conditions T_r and P_r according to the following relation:

$$\begin{aligned}\Delta\bar{G}^\circ_{fT,P} - \Delta\bar{G}^\circ_{fT_r,P_r} &= -\bar{S}^\circ_{T_r,P_r}(T-T_r) \\ &- c_1\left(T\ln\frac{T}{T_r} - T + T_r\right) + a_1(P-P_r) \\ &+ a_2\ln\left(\frac{2600+P}{2600+P_r}\right) \\ &- c_2\left[\left(\frac{1}{T-228} - \frac{1}{T_r-228}\right)\left(\frac{228-T}{228}\right)\right. \\ &\left.- \left(\frac{T}{(228)^2}\right)\ln\frac{T_r(T-228)}{T(T_r-228)}\right] + \left(\frac{1}{T-228}\right) \\ &\times \left[a_3(P-P_r) + a_4\ln\left(\frac{2600+P}{2600+P_r}\right)\right] \\ &+ \omega\left[Y_{P_r,T_r}(T-T_r) + \left(\frac{1}{\varepsilon_{TP}} - 1\right) - \left(\frac{1}{\varepsilon_{T_rP_r}} - 1\right)\right]\end{aligned} \tag{5}$$

wherein Y and ε refer to dielectric properties of H_2O tabulated by H. C. Helgeson and D. H. Kirkham [*Am. J. Sci.* **274**, 1089 (1974)] and ω is the solute's Born coefficient. Helgeson-Kirkham-Flowers (HKF) parameters for AuHS $(H_2S)_3{}^0$(aq) at T_r = 298.15 K and P_r = 1 bar are as follows: $\Delta\bar{G}^\circ_{fT_r,P_r} = -38{,}416$ cal/mol, $\Delta\bar{H}^\circ_{fT_r,P_r} = -47{,}973$ cal/mol, $\bar{S}^\circ_{T_r,P_r} = 120.77$ cal/mol-K, a_1 = 1.0620 cal/mol-bar, $a_2 = 11.39 \times 10^2$ cal/mol, a_3 = 0.0028 cal-K/mol-bar, $a_4 = -3.250 \times 10^4$ cal-K/mol, c_1 = 42.5614 cal/mol-K, $c_2 = 9.29 \times 10^4$ cal-K/mol, $\omega = -0.001 \times 10^5$ cal/mol. With the SUPCRT92 database, these parameters yield values of log K for Eq. 3 at 400° to 725°C that are within 0.002 log unit of the log K values given by Eq. 4 and the A, B, C, and D regression parameters in (*21*).
24. In Fig. 2, the contours for gold solubility as the AuHS°(aq) complex were generated from HKF equation-of-state parameters derived in this study from the experimental data of Gibert *et al.* (*31*) at 350°, 400°, and 450°C, 50 MPa, from that of Zotov (*32*) at 400°C, 50 MPa, and from experiments at 25°C and 0.1 MPa [P. J. Renders and T. M. Seward, *Geochim. Cosmochim. Acta* **53**, 245 (1989)]. In the $\Delta\bar{G}^\circ_{fT,P}$ equation given in (*23*), parameters for $AuHS^0$(aq) at T_r = 298.15 K and P_r = 1 bar are $\Delta\bar{G}^\circ_{fT_r,P_r} = +8605$ cal/mol, $\Delta\bar{H}^\circ_{fT_r,P_r} = +10{,}644$ cal/mol, $\bar{S}^\circ_{T_r,P_r} = 42.344$ cal/mol-K, a_1 = 0.68093 cal/mol-bar, $a_2 = 4.7412 \times 10^2$ cal/mol, a_3 = 3.3739 cal-K/mol-bar, $a_4 = -2.975 \times 10^4$ cal-K/mol, c_1 = −0.001 cal/mol-K, $c_2 = -2.5937 \times 10^4$ cal-K/mol, and $\omega = -0.0005 \times 10^5$ cal/mol. With the SUPCRT92 database, these parameters yield log K values for gold dissolution as $AuHS^0$(aq) within the experimental uncertainties at 25° to 450°C, 0.1 to 50 MPa.
25. M. Meyer and R. Saager, *Mineral. Deposita* **20**, 284 (1985); J. D. Greenough and B. J. Fryer, *Proc. Ocean Drill. Program Sci. Results* **115**, 71 (1990); S. Togashi and S. Terashima, *Geochim. Cosmochim. Acta* **61**, 543 (1997).
26. E. J. Mikucki and J. R. Ridley, *Mineral Deposita* **28**, 469 (1993).
27. At 370-MPa P_{H_2O} and 625°C, water saturated with LAPM has fugacities $f_{H_2} = 0.91$ MPa and $f_{H_2S} = 2.2$ MPa, according to thermodynamic data [Z. D. Sharp, E. J. Essene, W. C. Kelly, *Can. Mineral.* **23**, 517 (1985); P. B. Barton Jr. and B. J. Skinner, in *Geochemistry of Hydrothermal Ore Deposits*, H. L. Barnes, Ed. (Wiley, New York, 1979), pp. 278–403]. But $f_{H_2} = 0.03$ MPa and $f_{H_2S} = 4.1$ MPa at the same P and T on the PMP buffer (Table 1, run 6). By the stoichiometry of Eq. 3, these fugacity changes cause the gold saturation requirement to drop from ~761 ± 107 ppm Au (PMP, Table 1, run 6) to ~14 ± 7 ppm Au on the LAPM buffer.
28. F. Robert, A.-M. Boullier, K. Firdaous, *J. Geophys. Res.* **100**, 12 (1995); J. J. Wilkinson and J. D. Johnston, *Geology* **24**, 395 (1996).
29. R. W. Henley and A. McNabb, *Econ. Geol.* **73**, 1 (1978).
30. G. N. Phillips, T. Zhou, R. Powell, *S. Afr. J. Geol.* **100**, 393 (1997).
31. F. Gibert, M.-L. Pascal, M. Pichavant, *Geochim. Cosmochim. Acta* **62**, 2931 (1998).
32. A. V. Zotov, personal communication, cited by (*31*).
33. D. A. Sverjensky, J. J. Hemley, W. M. D'Angelo, *Geochim. Cosmochim. Acta* **55**, 989 (1991).
34. D. A. Sverjensky, E. L. Shock, H. C. Helgeson, *ibid.* **61**, 1359 (1997).
35. H. C. Helgeson, D. H. Kirkham, G. C. Flowers, *Am. J. Sci.* **281**, 1249 (1981); V. A. Pokrovskii and H. C. Helgeson, *Chem. Geol.* **137**, 221 (1997).
36. The buffer equilibrium FeS(c) + H_2S(g) = FeS_2(c) + H_2(g), which establishes the ratio a_{H_2}/a_{H_2S} (compare x- and y-axis scales in Fig. 1), has a small uncertainty in its γ_{FeS} and log K (*16*). That uncertainty could permit the plotted points to shift systematically by a small constant to error-free locations, meaning the x- and y-axis scales could slide by addition of small constants (vector components of the former). But the relative locations of the points and the slopes are unresponsive to plausible ranges of systematic error in log K on these isothermal, isobaric plots.
37. L. G. Benning and T. M. Seward, *Geochim. Cosmochim. Acta* **60**, 1849 (1996).
38. On the PMP buffer, the fluid's m_{H_2S} rises a billionfold from $10^{-8.2}$ at 25°C to ~15.6 m at 725°C, 110 MPa (*15*). Extreme T dependence of sulfide ligand availability evidently imposes a T trend on coordination number in Au^+ thio-complexes. Tetrahedral coordination of Au^+ with S as SH^- or $SH_2{}^0$ has not been reported in 25°C spectroscopic studies but is indicated by our $AuSH(SH_2)_3{}^0$(aq) stoichiometry. Only linear twofold coordination has been reported in H-S-O complexes of Au^+, but tetrahedral complexes of Au^+ with neutral ligands comprising $AsH_3{}^0$ and $SbH_3{}^0$ are known [R. J. Puddephatt, in *Comprehensive Coordination Chemistry*, F. Wilkinson, R. D. Gillard, J. A. McCleverty, Eds. (Pergamon, Oxford, UK, 1987), vol. 5, pp. 861–913]. Comparisons of Au^+ stereochemistry with Ag^+ and the iso-electronic Hg^{2+} ion are instructive: As $m_{Cl^-(aq)}$ increases, linear $AgCl_2{}^-$(aq) transforms to tetrahedral $AgCl_4{}^{-3}$(aq). Cyanides and ammines of Ag and Hg also undergo linear-to-tetrahedral transitions as ligand supply increases [R. J. Lancashire, in *Comprehensive Coordination Chemistry*, F. Wilkinson, R. D. Gillard, J. A. McCleverty, Eds. (Pergamon, Oxford, UK, 1987), vol. 5, pp. 775–860; N. N. Greenwood and A. Earnshaw, *Chemistry of the Elements* (Pergamon, Oxford, UK, 1984)].
39. Continuous black contours in Fig. 2 represent gold solubility through the reaction Au(c) + $1\frac{1}{8}$ FeS_2 + $\frac{5}{4}$FeS + $\frac{7}{2}H_2O$ = $AuHS(H_2S)_3{}^0$(aq) + $\frac{7}{8}Fe_3O_4$, for which the sizable negative $\Delta_r V^\circ$ is increasingly negative as H_2O expands with decreasing P or increasing T, widening the separation of isobars as P decreases or T increases. Continuous gray contours represent the reaction Au(c) + $\frac{5}{8}FeS_2$ + $\frac{1}{2}H_2O$ = $AuHS^0$(aq) + $\frac{1}{4}$FeS + $\frac{1}{8}Fe_3O_4$, which has a small positive $\Delta_r V^\circ$ at elevated P, approaching zero (even negative at high T) as H_2O expands with decreasing P or increasing T, narrowing the spacing of $AuHS^0$(aq) solubility isobars.
40. For Fig. 2, calculated pH values for the OMQ buffer (*33*) in 1 m KCl + HCl are pH = 4.1 at 250°, 4.2 at 300°, 4.4 at 350°, and 4.65 at 400°C, with P_{sat}. At such acidic pH, $m_{HS^-}/m_{H_2S} \approx 10^{-3}$ to 10^{-5} (*15*), making $Au(HS)_2{}^-$(aq) subordinate to complexes requiring fewer HS^- ions.
41. C. H. Gammons and A. E. Williams-Jones, *Geochim. Cosmochim. Acta* **59**, 3453 (1995).
42. ———, *Econ. Geol.* **92**, 45 (1997).

43. We thank S. Eggins, W. Hibberson, L. Kinsley, H. O'Neill, M. Shelley, and N. Ware for technical assistance in experimental and analytical aspects of this study and B. L. N. Kennett for supporting development of the analytical facilities. D. Ellis kindly shared his cold-seal laboratory. Comments by A. Berry, I. Campbell, C. Heinrich, S. Kesson, M. Palin, D. Sverjensky, and anonymous reviewers clarified the presentation.

19 January 1999; accepted 30 April 1999